

JGR Atmospheres

RESEARCH ARTICLE

10.1029/2019JD031206

Key Points:

- We define a new diagnostic diffusivity framework to interpret the midlatitude circulation response to climate change
- Warming shifts diffusivity poleward, in part following moist static energy gradient changes not fully explained by Clausius-Clapeyron
- Changes in the position and intensity of maximum midlatitude diffusivity are correlated with storm track metrics such as eddy kinetic energy

Supporting Information:

· Supporting Information S1

Correspondence to: T. A. Mooring, tmooring@alum.mit.edu

Citation:

Mooring, T. A., & Shaw, T. A. (2020). Atmospheric diffusivity: A new energetic framework for understanding the midiatitude circulation response to climate change. Journal of Geophysical Research: Atmospheres, 125, e2019ID031206. https://doi.org/10. 1029/2019JD031206

Received 19 JUN 2019 Accepted 6 DEC 2019 Accepted article online 11 DEC 2019

Atmospheric Diffusivity: A New Energetic Framework for Understanding the Midlatitude Circulation Response to Climate Change

Todd A. Mooring^{1,2} and Tiffany A. Shaw¹

¹Department of the Geophysical Sciences, University of Chicago, Chicago, IL, USA, ²Now at Department of Earth and Planetary Sciences, Harvard University, Cambridge, MA, USA

Abstract The midlatitude circulation response to climate change is not well understood. Within an energetic framework the circulation is connected to the atmospheric diffusivity. Here we define a novel diagnostic diffusivity framework as a tool for interpreting changes in the midlatitude atmospheric circulation. The diffusivity is computed by dividing the zonally and vertically integrated transient eddy moist static energy (MSE) transport by the zonal-mean 925 hPa MSE gradient, and we investigate the diffusivity response to global-scale sea surface temperature (SST) perturbations in aquaplanet and Atmospheric Model Intercomparison Project (AMIP) general circulation model simulations. The midlatitude diffusivity maximum shifts poleward with increasing SST in both the aquaplanet simulations and Southern Hemisphere winter of the AMIP simulations. Our framework indicates that this diffusivity shift is associated with Ferrel circulation and 925 hPa MSE gradient changes, rather than with total MSE transport changes. The MSE gradient-related shift cannot be understood purely in terms of Clausius-Clapeyron changes in specific humidity following the global-mean temperature response, because atmospheric temperature gradients change significantly even when SST gradients are held fixed. The intensity of the diffusivity maximum also increases with SST for the aquaplanet configuration but is relatively insensitive to SST for AMIP Southern Hemisphere winter. Additional energy balance model experiments suggest that while diffusivity changes caused by SST perturbations can be large, their effect on zonal-mean temperature is minor. Finally, the latitudes and intensities of the diffusivity maxima are strongly correlated with the same properties of the zonal-mean eddy kinetic energy maxima. However, existing theories cannot adequately explain these linear relationships.

1. Introduction

Comprehensive climate models project that the atmospheric circulation will change in response to global warming. Simulations from such models exhibit a number of robust features, including a poleward shift of the Hadley cell edge, storm track, and eddy-driven jet (Shaw et al., 2016; Vallis et al., 2015). They also show changes in storm track intensity as indicated by changes in eddy kinetic energy (EKE) or transient eddy moist static energy (MSE) transport (O'Gorman, 2010; Shaw et al., 2018). However, achieving a dynamical understanding of these phenomena has proven difficult (Shaw, 2019).

Fundamentally, changes in greenhouse gas and aerosol levels alter the climate by changing the atmospheric energy budget. This suggests that characterizing the atmospheric circulation in terms of its energy-transporting properties may be a promising approach to understanding the circulation's response to radiative forcing (e.g., Barpanda & Shaw, 2017; Shaw et al., 2018). Tropospheric specific humidity is also expected to exhibit a basically Clausius-Clapeyron response to temperature changes (e.g., Held & Soden, 2006). These water vapor changes potentially also provide a thermodynamic source of insight into circulation changes: Shaw and Voigt (2016) attempted to use an assumption of fixed relative humidity to compute, among other things, changes in the latitudes of the Hadley cell edge and the maxima of dry static and latent energy transports.

Within an energy budget-based diagnostic framework, the atmospheric circulation is most naturally quantified as a diffusivity. Diffusion has also long been used as a parameterization of atmospheric circulation in prognostic energy balance models (EBMs) of the climate system (e.g., Flannery, 1984; Sellers, 1969), providing additional motivation for diagnostic analyses of diffusivity (Pierrehumbert, 2005). Many attempts

©2019. American Geophysical Union. All Rights Reserved.

MOORING AND SHAW 1 of 20



have been made to theoretically compute appropriate values for the diffusivity (e.g., Barry et al., 2002). Shaw and Voigt (2016) sought to calculate diffusivity changes in response to a globally uniform sea surface temperature (SST) increase using Coupled Model Intercomparison Project phase 5 aquaplanet simulations via assumptions of fixed relative humidity and fixed total meridional MSE transport, while some diagnostic work (Kushner & Held, 1998) suggests a relationship between diffusivity and the eddy stream function variance.

Here we investigate diffusivity changes in response to global-scale SST perturbations, as simulated by an atmospheric general circulation model (AGCM). The investigation has two main aspects. First, we define a new diffusivity framework based on the MSE budget and use it to relate changes in diffusivity to changes in the time mean atmospheric state and meridional energy fluxes. This allows us to improve upon Shaw and Voigt (2016) with a more systematic analysis of the significance of Clausius-Clapeyron near-surface specific humidity changes for overall circulation change. Second, we seek a relationship between our diffusivity and other dynamical quantities more explicitly related to traditional definitions of the storm track.

We adopt a diffusivity definition similar (but not identical—see section 2.1) to Shaw and Voigt (2016), computing it as the ratio of the transient eddy MSE flux to the 925 hPa MSE gradient. However, the overall framework primarily builds on the studies of Barpanda and Shaw (2017) and Shaw et al. (2018), which defined the midlatitude storm track as the maximum in transient eddy MSE transport. The advantage of the present diffusivity framework over the eddy MSE transport-based framework is that the latter cannot be used to investigate possible influences of the thermodynamic mean state itself on storm track behavior. This is because, to the extent that transient eddy MSE transport can be expressed as the product of a diffusivity and a mean state MSE gradient, any storm track properties diagnosed directly from the transient eddy MSE transport field as in Barpanda and Shaw (2017) and Shaw et al. (2018) will be influenced by both the diffusivity and the mean state.

It must be emphasized that our diffusivity is entirely diagnostic in nature, unlike studies that explicitly invoke a dynamical argument for the functional form of the diffusivity (e.g., Held & Larichev, 1996; Kushner & Held, 1998; Stone, 1973). While this approach appears to be relatively uncommon, similar methods were previously used by Pierrehumbert (2005) to analyze general circulation model simulations of the snowball Earth and are implicitly taken in EBM studies in which diffusivities are tuned to match data or more complex models (e.g., Frierson et al., 2007; Hwang & Frierson, 2010; Sellers, 1969). Indeed, we expand on these earlier studies by using an EBM to explore the implications of the diffusivity changes diagnosed from our general circulation model simulations. However, our core objective is to relate the diffusivity changes to other storm track metrics: in this study, vertically integrated EKE and a rescaled form of the 925 hPa root-mean-square (RMS) eddy stream function.

The main body of this paper is divided into four sections. We more formally present the details of our methodology, including the diffusivity framework and the EBM, in section 2. The general circulation model simulations we analyze are described in section 3. Section 4 describes how meridional profiles of diffusivity change with global temperatures, summarizing their properties in terms of the positions and intensities of midlatitude maxima. Section 5 documents the relationships between diffusivity and the two other storm track metrics, as well as exploring the implications of the diagnosed diffusivity changes for EBM simulations. A discussion and conclusions are presented in a final section.

2. Methods

Here we describe our two main analysis techniques. In section 2.1, we formally define the diffusivity and explain how its changes with climate can be related to different atmospheric processes. We then present in section 2.2 the EBM we use to investigate the effects of the diffusivity changes.

2.1. Diffusivity Definition and Framework

Our choice to compute a diffusivity diagnostically, as the ratio of a transport and a gradient, is similar to that of Pierrehumbert (2005). We define D, the atmospheric transient eddy MSE diffusivity in units of kg/s, as

$$D = -\frac{H}{G} \tag{1}$$

where H is the multiannual- and seasonal-mean zonally and vertically integrated MSE transport by transient eddies and the transient eddies are defined as anomalies from monthly means. For maximum accuracy,

MOORING AND SHAW 2 of 20

H and other transports are computed using the general circulation model's native vertical coordinate as described in Appendix A and indeed H is more rigorously defined in (A4). However, it is worth clarifying here that the transported quantity (MSE) is $m = c_p T + gz + Lq$. H has units of W/m—we opted to normalize the transport in units of W by $2\pi a$ where a is the Earth's radius. It is appropriate to evaluate H over the full depth of the atmosphere because it is vertically integrated transports that are connected to the net energy input to the atmosphere (Neelin and Held, 1987).

G is the multiannual- and seasonal-mean 925 hPa MSE gradient in units of J/kg/m, formally defined as

$$G = \frac{1}{a} \frac{\partial m_s}{\partial \phi} \tag{2}$$

where ϕ is the latitude. m_s is simply the zonal mean of m evaluated at 925 hPa, with the zonal average taken over longitudes for which 925 hPa is above ground. Eddy MSE transports are relatively intense in this part of the atmosphere, and our decision to evaluate G near the surface is similar to previous work with EBMs (Frierson et al., 2007; Hwang & Frierson, 2010). (We also repeated a subset of our analyses with G evaluated at 850 hPa and generally obtained qualitatively similar results.) Furthermore, G can be separated into components due to dry static energy G_d and latent energy G_l according to

$$G = G_d + G_l \tag{3}$$

where $G_d = (1/a) \partial (c_p T + gz) / \partial \phi$ and $G_l = (1/a) \partial (Lq) / \partial \phi$.

The diffusivity in (1) is conceptually distinct from that used in Shaw and Voigt (2016) and in many EBM studies (e.g., Hwang & Frierson, 2010), in which the diffusivity is based on total atmospheric MSE transport. However, use of a transient eddy-based diffusivity eases comparisons to the eddy MSE transport maximum-based storm tracks of Barpanda and Shaw (2017) and Shaw et al. (2018). Following those two studies, we decompose total MSE transport H_{tot} into transports by the mean meridional circulation H_{mmc} , stationary eddies H_{se} , and transient eddies H using monthly and zonal averages. Seasonal means underlying the computation of D in (1) are calculated from relevant monthly means. Upon rearranging the decomposition for transient eddy MSE transport, we have

$$H = H_{tot} - H_{mmc} - H_{se} \tag{4}$$

which will be helpful for relating the diffusivity to other aspects of the circulation.

To understand total MSE transport-related intensity changes, we use the relationship between H_{tot} , zonal-mean energy input to the atmosphere EIA, and zonal-mean rate of energy storage in the atmosphere $\partial h/\partial t$:

$$H_{tot}(\phi) = a \int_{-\pi/2}^{\phi} \left(EIA(\hat{\phi}) - \partial h(\hat{\phi}) / \partial t \right) \cos \hat{\phi} \, d\hat{\phi}$$
 (5)

The integrand has units of W/m² and in Barpanda and Shaw (2017) and Shaw et al. (2018) is referred to as "net energy" and "net energy input," respectively. Energy input to the atmosphere can be subdivided according to

$$EIA = SWABS + SHF - OLR$$
(6)

where SWABS is shortwave absorption within the atmosphere, SHF is surface heat flux into the atmosphere (the sum of sensible, latent, and surface longwave fluxes), and OLR is outgoing longwave radiation (Donohoe & Battisti, 2013). Note that we remove global means from the components of EIA prior to computing the MSE transports they induce, to prevent implied MSE transports through the poles.

Changes in diffusivity δD relative to some climatological state can be decomposed into contributions from transient eddy MSE transport and 925 hPa MSE gradient as follows:

$$\delta D = -\frac{\delta H}{G} + \frac{H \delta G}{G^2} = \delta D_H + \delta D_G \qquad (7)$$

MOORING AND SHAW 3 of 20

Table 1			
Latitude Ranges Used for Diffusivity,	Eddy Kinetic Energy,	and Rescaled wome	Maximum Searches

Configuration	Terms	Latitude range
AQUA/AQUA-SO	δD_{Htot} , δD_{Hmmc} , δD_{Hse} , δD_{G} , $\delta D_{Hmmc,dyn}$, $\delta D_{Hmmc,thr}$,	20-60°
	$\delta D_{Hmmc,nln}$, δD_{Gl} , δD_{Gd} , δD_{G} (true T, fixed RH),	
	δD_G (nominal T, fixed RH), δD_{SWARS} , δD_{SHF} , δD_{OLR} ,	
	Atmospheric storage, δD_{LAT} , δD_{SENS} , δD_{LWSFC} ,	
	D seasonal variability, eddy kinetic energy, rescaled ψ_{RMS}	
AQUA/AQUA-SO	δD	20-58°
AQUA/AQUA-SO	δD (linear estimate)	22-58°
AMIP/AMIP-SO	δD (linear estimate), δD_{Htot} , δD_{Hmmc} , δD_{Hse} ,	20-50°S
	$\delta D_{Hmmc,dyn}$, $\delta D_{Hmmc,thr}$, $\delta D_{Hmmc,nln}$, δD_{Gl} ,	
	δD_G (nominal T, fixed RH), δD_{SWABS} , δD_{SHF} , δD_{OLR} ,	
	Atmospheric storage, δD_{LAT} , δD_{SENS} , δD_{LWSFC} ,	
	D seasonal variability	
AMIP/AMIP-SO	δD , δD_G , δD_{Gd} , δD_G (true T, fixed RH)	20-48°S
AMIP/AMIP-SO	Eddy kinetic energy, rescaled ψ_{RMS}	20-60°S

Note. Term names are generally as in figure legends. Search ranges for internal variability quantification and terms not shown in figures are included as well. AMIP search ranges are truncated to reduce the frequency of physically inappropriate abrupt jumps of the diagnosed diffusivity maximum to high latitudes as SST is changed. For example, the -8 K experiment has two local maxima (Figure C1b), and the lower-latitude maximum appears to be more closely related to the (single) maximum found in warmer experiments—limiting the δD search range to $20-48^{\circ}$ S is necessary to capture the equatorward maximum. Similar behavior occurs for AQUA, but low-latitude truncations are also used to prevent unreasonably far equatorward identifications of diffusivity slope minima in the +6 K and +8 K experiments (Figure C1c). The δD (linear estimate) search ranges are relevant only to Figures C1c and C1d, while the eddy kinetic energy and rescaled ψ_{RMS} search ranges are relevant only to Figure 6.

where δD_H and δD_G are diffusivity increments associated with changes in H and G. δD_H and δD_G can be decomposed using (4) and (3):

$$\delta D_{H} = -\frac{\delta H_{tot}}{G} + \frac{\delta H_{mmc}}{G} + \frac{\delta H_{se}}{G} = \delta D_{Htot} + \delta D_{Hmmc} + \delta D_{Hse}$$
 (8)

$$\delta D_G = \frac{H\delta G_d}{G^2} + \frac{H\delta G_l}{G^2} = \delta D_{Gd} + \delta D_{Gl} \qquad (9)$$

 δD_{Hiot} , δD_G , δD_{Gd} , and δD_{Gl} can be defined as thermodynamic in nature, as they can be computed without explicit reference to changes in atmospheric motion (via energy budget closure arguments, for δD_{Hiot}). Furthermore, δD_{Hmmc} can itself be divided into dynamic and thermodynamic components ($\delta D_{Hmmc,dyn}$ and $\delta D_{Hmmc,thr}$) following work on the moisture budget (Seager et al., 2010) as described in Appendix B. All other perturbations (δD_{Hse} and indeed δD_H and δD_{Hmmc} prior to their separation into various components) are classified as dynamic in nature.

Following Barpanda and Shaw (2017) and Shaw et al. (2018) we will focus much of our work on changes in the positions and intensities of midlatitude diffusivity maxima in the AGCM simulations of global temperature change described in section 3. We assign these changes to various components of H and G using method 2 of Barpanda and Shaw (2017), which is described in more detail in Appendix C. Note that in the limit of spatially constant G and $\delta G = 0$ we would recover the Barpanda and Shaw (2017) results on storm track position exactly and the Shaw et al. (2018) storm track intensity results up to a factor of G. Alternatively, we recover the Shaw and Voigt (2016) diffusivity definition from (1) in the limit in which $H_{mmc} = H_{se} = 0$.

We impose latitude restrictions on the diffusivity maximum search, typically 20–60° (for aquaplanet simulations) or 20–50°S (for AMIP simulations)—the latitude restrictions are described more fully in Table 1. The search identifies the absolute maximum in the region of interest, but if no maximum exists we define the "maximum" as the latitude at which $|\partial D/\partial \phi|$ is minimized. All MSE transport profiles computed from model level data were filtered as in Sardeshmukh and Hoskins (1984, their equation 9 with coefficients n_0 = 21 and r = 1) and then interpolated to a 0.1° grid before computing diffusivities, and gradient profiles

MOORING AND SHAW 4 of 20



were processed similarly—this smooths the diffusivity profiles in an attempt to make the maximum search more robust.

2.2. EBM

The EBM we use is a modified version of the one described by Hwang and Frierson (2010). Our EBM computes 925 hPa MSE from the temperature and specified spatially varying relative humidity and geopotential height fields—in contrast, Hwang and Frierson (2010) evaluated MSE at the surface and assumed a spatially constant relative humidity. But as in Hwang and Frierson (2010), we assume the clear sky OLR is a linear function of the temperature and specify all other contributions to the net MSE generation rate.

The exact definition of diffusivity is the most notable difference of our EBM from the Hwang and Frierson (2010) version: If we choose the diffusivity to follow the spatially varying D as diagnosed from general circulation model simulations using (1), then the EBM-computed MSE transport represents eddy MSE transport only, and we must additionally specify the convergence of the MSE transport by the time mean flow in order to properly close the EBM's MSE budget. Alternatively, we can close the MSE budget and make the EBM's total MSE transport diffusive by taking the diffusivity to follow

$$D_{tot} = -\frac{H_{lot}}{G}$$
(10)

where H_{tot} and G are again diagnosed from general circulation model simulations. This latter approach is more similar to Hwang and Frierson (2010)'s original model, but note that this D_{tot} still needs to be divided by a factor of $\cos \phi$ to be rendered directly comparable to the p_sD/g term that appears in Hwang and Frierson (2010) equation (A1). Both versions of our EBM are solved on a 0.1° grid using an iterative algorithm, with the 925 hPa temperature field adjusted until the net heating rate of each latitude band of the model is reduced to <0.001 W/m².

3. Simulations

We primarily analyze atmospheric diffusivity in prescribed-SST aquaplanet and Atmospheric Model Intercomparison Project (AMIP)-style simulations with ECHAM6, the AGCM of the MPI-ESM-LR coupled climate model (Stevens et al., 2013). The two configurations will be referred to as AQUA and AMIP, respectively, and constitute two steps in a model hierarchy (e.g., Held, 2005; Shaw et al., 2016) intended to build up understanding of the zonally symmetric midlatitude circulation response to warming. The SSTs for the AQUA and AMIP control simulations are prescribed according to the interhemispherically symmetric Qobs distribution of Neale and Hoskins (2000) and the AMIP protocol (Gates, 1992), respectively. The reasonableness of using observation-based SSTs for the AMIP-style simulations is obvious, while Neale and Hoskins (2000) in fact proposed a family of possible SST distributions for idealized aquaplanet simulations. Their Qobs distribution is relatively close to observations and is thus suitable for our purposes (Neale & Hoskins, 2000).

The diffusivity response to climate change is simulated by perturbing the control SST fields from -8 to +8 K in 2 K increments, subject to the constraint that SSTs are never permitted to fall below 271.38 K—note that this produces some nonuniformity in the SST anomaly fields of the cooled simulations. All other forcings (greenhouse gases, sea ice, etc.) are held fixed. Imposing temperature changes using the SST field rather than actual radiative forcing agents is reasonable because previous work found that the midlatitude jet response to increased CO_2 is primarily due to SST changes (Grise & Polvani, 2014; He et al., 2014). Nevertheless, to make sure that our results are not somehow an artifact of the prescribed SSTs we repeat parts of the analysis using two pairs of simulations with prognostic (slab ocean) SSTs. One of the pairs (referred to as AQUA-SO) consists of aquaplanet simulations while the other (AMIP-SO) uses realistic geography. Each pair consists of a control simulation with 359 ppmv CO_2 and a perturbation simulation with 1436 ppmv (quadrupled) CO_2 . For both pairs, the slab oceans are 50 m deep. There is no ocean heat transport in the AQUA-SO simulations, while the prescribed ocean heat transport (Q-flux) in the AMIP-SO simulations was chosen to reproduce the ocean surface heat fluxes of the AMIP control simulation.

All of the simulations have a resolution of T63 ($\sim 1.9^{\circ}$) in the horizontal and 47 levels in the vertical. The AQUA and AQUA-SO simulations are run for 10 years each with perpetual equinox insolation, while the AMIP and AMIP-SO simulations use realistic seasonal insolation and are run for 30 years. To focus attention on climates that are relatively zonally symmetric and to limit the scope of the analysis, we present only

MOORING AND SHAW 5 of 20

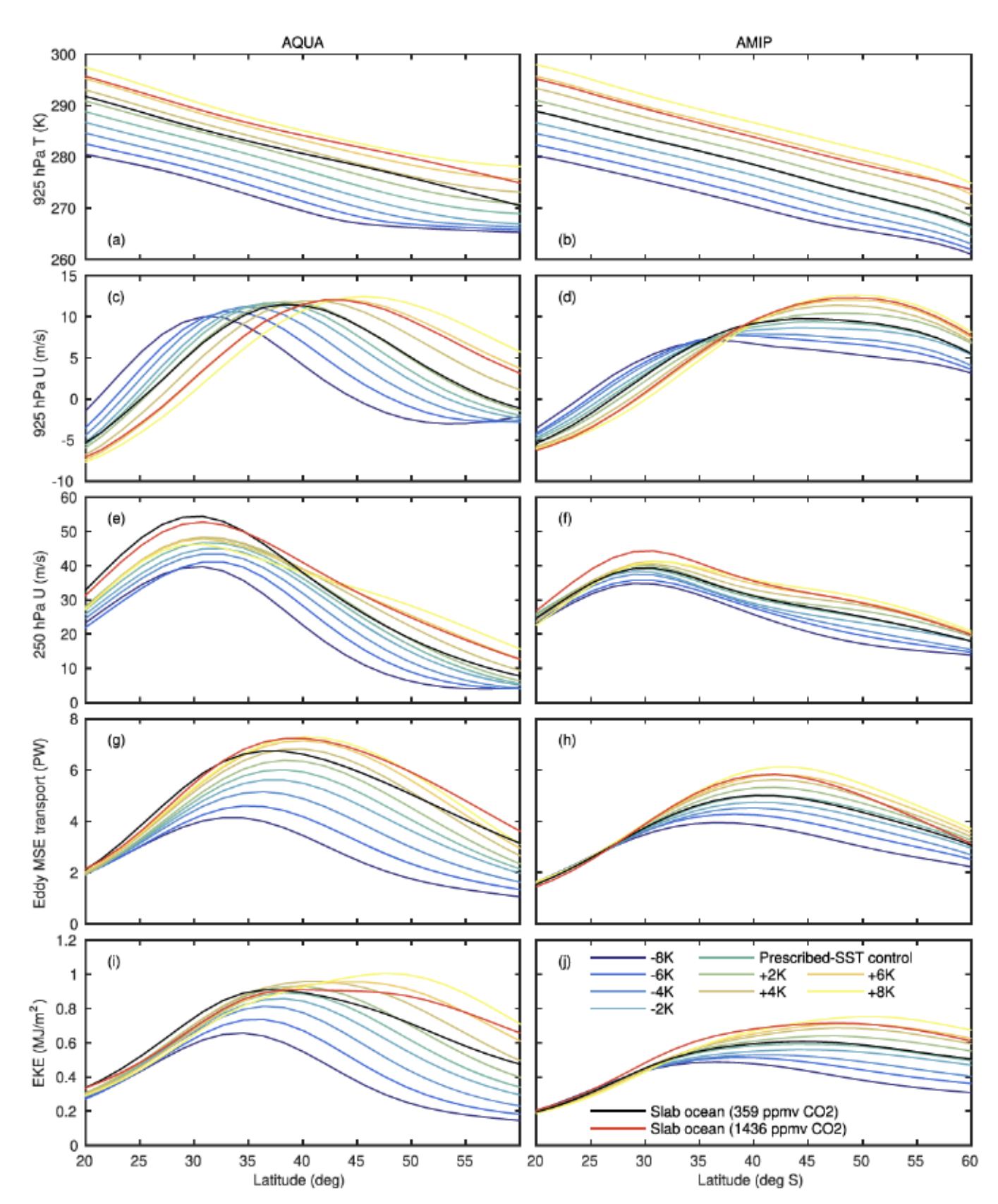


Figure 1. A selection of midlatitude mean state and eddy fields from the ECHAM6 simulations analyzed in this paper. Aquaplanet (AMIP-style) results are shown in the left (right) column—specific variables are 925 hPa temperature (a, b), 925 hPa zonal wind (c, d), 250 hPa zonal wind (e, f), zonally integrated eddy MSE transport (g, h), and zonal-mean eddy kinetic energy (i, j). The AMIP-style results are for SH winter; see main text for more details.

MOORING AND SHAW 6 of 20

Southern Hemisphere (SH) winter results from the AMIP and AMIP-SO simulations in the main paper. We repeated a subset of our analyses for the other SH seasons and briefly present the results in the supporting information (Text S1). In general, they are qualitatively similar to the winter results. The zonal asymmetry of the Northern Hemisphere circulation response to warming is well known (Grise and Polvani, 2014; Simpson et al., 2014), and thus we do not attempt to analyze it with our zonally symmetric framework.

To frame our analysis of diffusivity and its variations with SST, we survey the midlatitude circulations of our simulations in Figure 1. The inter-simulation differences in 925 hPa temperature are relatively spatially uniform (Figures 1a and 1b), consistent with the imposed SST perturbations—however, note that the minimum-SST constraint mentioned above causes the temperature profiles in the cooler AQUA simulations to begin to converge poleward of $\sim 45^{\circ}$ latitude. Agreement of 925 hPa temperature between the prescribed-SST and slab ocean experiments is generally better with realistic geography than with a global ocean, particularly at high latitudes (not shown). This is presumably because of the explicit attempt to include reasonable ocean heat transports in AMIP-SO but not in AQUA-SO. (Nor are the slab ocean simulations constrained to have a specific minimum SST.)

There is also a dynamical response to the imposed changes in SST or CO₂, as seen in zonal winds in the lower troposphere (925 hPa, Figures 1c and 1d) and near the tropopause (250 hPa, Figures 1e and 1f). Poleward shifts of the near-surface jets with increasing SST are evident in the prescribed-SST experiments and qualitatively reproduced by the slab ocean experiments (Figures 1c and 1d). The higher altitude results are perhaps best summarized as a jet intensification with warming—however, the jet intensity changes are not always monotonic with SST (Figure 1e).

Finally, we examine some basic statistics of midlatitude eddy activity: zonally integrated eddy MSE transport (Figures 1g and 1h) and zonal-mean EKE (Figures 1i and 1j). The eddy MSE transport maxima generally intensify with increasing SST and tend to shift poleward, at least for the prescribed-SST simulations (Figures 1g and 1h). EKE also usually increases with SST, albeit not monotonically at all latitudes (Figures 1i and 1j). Furthermore, both metrics of eddy activity appear to respond more strongly to prescribed-SST changes for the AQUA simulations than for the AMIP simulations.

4. Response of Midlatitude Diffusivity Maxima to SST Change

We begin our primary analysis by quantifying diffusivity shifts and intensity changes in response to warming and cooling, connecting them to the thermodynamic and dynamic contributions described in section 2.1. To quantify the robustness of these forced diffusivity changes, we make comparisons to the unforced low-frequency variability of the AQUA and AMIP control simulations. Specifically, standard deviations of latitudes and magnitudes of diffusivity maxima are computed over 36 successive 90-day periods of the AQUA control run and 30 SH winters of the AMIP control run. Note also that for the AQUA and AQUA-SO simulations we average H and G values from both hemispheres prior to computing D and changes therein to obtain better statistics.

4.1. Diffusivity Shifts

A robust poleward shift of the diffusivity maximum with increasing SST is found for both prescribed-SST model configurations, but is notably larger in AQUA (red line, Figures 2a and 2b). According to the MSE diffusivity framework, changes in the mean meridional circulation (MMC) MSE transport (green line, Figures 2a and 2b) and MSE gradient (gold line, Figures 2a and 2b) dominate the diffusivity shift. Terms associated with changes in total (magenta line, Figures 2a and 2b) and stationary eddy MSE transport (blue line, Figures 2a and 2b) are generally smaller—the latter finding is consistent with the limited or absent zonal asymmetry of the boundary conditions. The residual (black line, Figures 2a and 2b) is often small relative to at least some linear terms of the decomposition.

The dynamic component of the MMC MSE transport diffusivity shift (cyan solid line, Figures 2c and 2d) is found to be much more important than the thermodynamic component (cyan dashed line, Figures 2c and 2d). The nonlinearities associated with separating changes in H_{mmc} into dynamic and thermodynamic parts are insignificant (not shown), consistent with previous work (Seager et al., 2010), as is the residual associated with separating the MMC-related diffusivity shift into the three physically meaningful components (black dotted line, Figures 2c and 2d). The midlatitude diffusivity maxima in our simulations are always located poleward of the Hadley cell edge as defined by the latitude where the 925 hPa zonal wind is 0 in the subtropics

MOORING AND SHAW 7 of 20

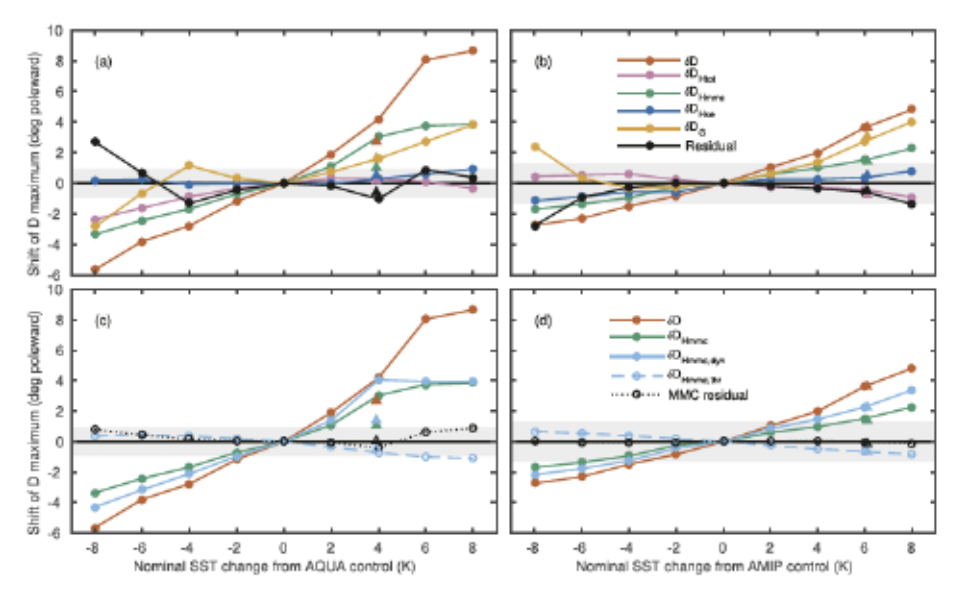


Figure 2. Components of midlatitude diffusivity shifts for AQUA (a, c) and AMIP (b, d) model configurations—AMIP results are for SH winter. The red line in all panels is the actual total shift of the diffusivity maximum. The other lines are components of this shift; see main text for descriptions. Gray shading in each panel is ±1 standard deviation of the internal variability of the latitude of the diffusivity maximum in the AQUA or AMIP control simulation, as appropriate. The triangles show the response to quadrupled CO₂ in the slab ocean model configuations AQUA-SO (a, c) and AMIP-SO (b, d).

(Shaw & Voigt, 2016), indicating that the MMC-linked diffusivity shift is associated with changes in the Ferrel cell.

Generally speaking, the diffusivity shift response to quadrupled CO_2 in the slab ocean simulations is similar to that of prescribed-SST simulations with comparable SST anomalies. The agreement between AMIP and AMIP-SO is particularly impressive—compare the triangles (AMIP-SO) with the lines (AMIP) in Figures 2b and 2d. For the aquaplanets, the overall poleward shift for AQUA-SO is 36% smaller than in the AQUA +4 K experiment (red triangle, Figure 2a). The MMC-related component of the AQUA-SO diffusivity shift (green triangle, Figure 2a) is only 34% as large as its AQUA counterpart, but as for AQUA the dynamic component of the MMC-related shift dominates over the thermodynamic component (cyan triangles, Figure 2c). As was the case for 925 hPa temperature (Figures 1a and 1b), the better agreement between the AMIP and AMIP-SO configurations may be because the prescribed ocean heat transport in the AMIP-SO simulations was chosen to match that implied by the AMIP control simulation, whereas the AQUA-SO simulations have no ocean heat transport at all and thus do not match the transport implied by the AQUA control simulation.

The MSE gradient-linked diffusivity shifts for AQUA and AMIP are a nonlinear function of SST, which suggests they might be related to Clausius-Clapeyron moistening with warming. In response to global warming, the latent energy gradient term (cyan solid line, Figures 3a and 3b) dominates. In contrast, the global cooling response in AMIP is dominated by the dry static energy gradient term (cyan dashed line, Figures 3a and 3b). For AQUA, the residual (black dotted line, Figures 3a and 3b) becomes so large in response to cooling that the relative roles of the dry static and latent energy gradient changes cannot be meaningfully quantified.

It is tempting to understand the latent energy gradient change component of the poleward diffusivity shift with warming in terms of a fixed 925 hPa temperature gradient and Clausius-Clapeyron moistening. However, the situation is more complex (Figures 3c and 3d). As described in section 2.1, the MSE gradient profiles (gold solid line, Figures 3c and 3d) are computed using the actual 925 hPa temperature and specific humidity profiles from the simulations. In more formal terms, this fact can be expressed as

$$m_s^{x} = c_p[T^x] + g[z^x] + L[q^x]$$
 (11)

where m_s has the same definition as in (2), the x superscripts identify the simulation, and the square braces denote zonal means. It is also possible to write (11) as

$$m_x^x = c_p[T^x] + g[z^x] + L[r^xq^*(T^x)]$$
 (12)

MOORING AND SHAW 8 of 20

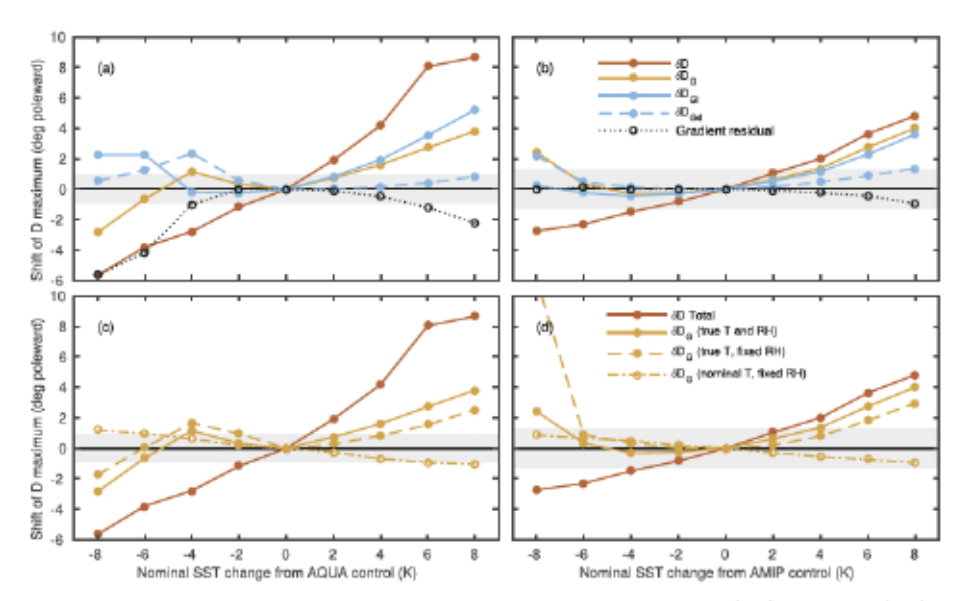


Figure 3. MSE gradient-related components of midlatitude diffusivity shifts for AQUA (a, c) and AMIP (b, d) model configurations. The red and gold solid lines and gray shading of all panels are as in Figure 2. Top row decomposes the MSE gradient-related shift (gold line) into components associated with the latent and dry static energy gradients and a residual. Bottom row presents two simplified estimates of the MSE gradient-related diffusivity shift (gold dashed and dash-dot lines); see main text for details. Note that the value of one of these estimates for the AMIP –8 K experiment is 11.1°. This abrupt shift is associated with replacement of a local maximum north of 40°S with one near 48°S.

where r and q^* are the (zonally varying) relative humidity and saturation specific humidity, respectively.

Alternatively, we can carry out the gradient calculation by assuming that relative humidity remains fixed at control simulation values. In other words, we redefine m_s^x according to

$$m_s^x = c_p[T^x] + g[z^x] + L[r^cq^*(T^x)]$$
 (13)

where the *c* superscript denotes a quantity evaluated from the relevant control simulation. This yields the gold dashed line of Figures 3c and 3d—the resulting estimated diffusivity shifts are qualitatively similar to the actual gradient-linked shifts, capturing the poleward shift with warming above the control runs and its nonmonotonicity with SST.

The success of the fixed relative humidity assumption does not mean that Clausius-Clapeyron moistening is the only important factor for explaining the MSE gradient-related diffusivity shifts. We explore the role of temperature gradient change by continuing to assume fixed relative humidity and also estimating the perturbed temperature fields by adding the globally uniform nominal SST perturbations (-8, -6, ..., +8 K) to the actual control run 925 hPa temperature fields. Quantitatively, this amounts to again redefining m_s^x as

$$m_s^x = c_n[T^c + n^x] + g[z^x] + L[r^cq^*(T^c + n^x)]$$
 (14)

where n^x is the nominal SST perturbation in simulation x. Temperature gradients are thus unchanged from their control run values, and the predicted diffusivity shifts turn out to be quite unrealistic (gold dash-dot line, Figures 3c and 3d). For experiments warmer than the control runs, the shifts are much too small and of the wrong sign. This implies that near-surface atmospheric temperature gradient changes are strongly related to the actual gradient-related diffusivity shifts (Shaw and Voigt, 2016)—since the SST gradient is unchanging (at least in the warmed simulations), 925 hPa temperature gradient change is evidently driven by circulation adjustment.

4.2. Diffusivity Intensity Changes

Diffusivity increases monotonically with SST for AQUA, but diffusivity changes are much smaller and nonmonotonic for AMIP (red line, Figures 4a and 4b). The most important component of diffusivity increase is associated with total MSE transport increase (magenta line, Figures 4a and 4b). The much weaker overall response of intensity for AMIP is mainly associated with opposite signs of the MMC-related response to

MOORING AND SHAW 9 of 20

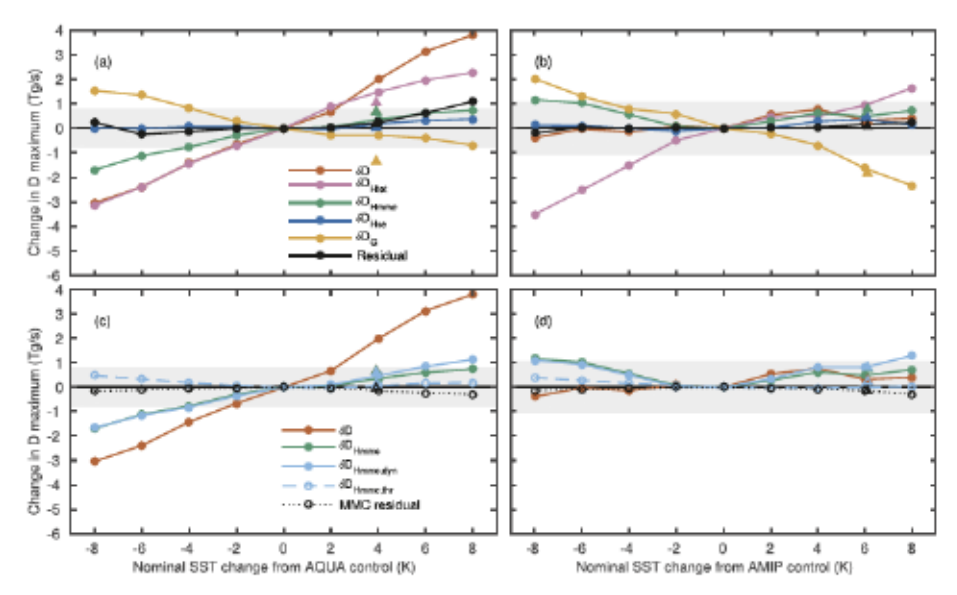


Figure 4. As in Figure 2, but for changes in diffusivity maximum intensity. The total intensity change marker for AQUA-SO (a, red triangle) and the total MSE transport-related intensity change marker for AMIP-SO (b, magenta triangle) are not visible because they are overlapped by MMC-related intensity change markers (a and b, green triangles).

cooling (green line, Figures 4a and 4b) and differences in total transport- and gradient-related responses to warming (magenta and gold lines, Figures 4a and 4b).

As mentioned in the previous subsection, the diffusivity maxima are located within the latitude range of the Ferrel cell. For AQUA, the (equatorward) Ferrel cell MSE transports generally become more intense with increasing SST while for AMIP their behavior is more complex and less monotonic (not shown). This last result is not inconsistent with the relatively linear dependence of the AMIP MMC-related diffusivity shift (green line, Figure 2b) on SST, because diffusivity (or MMC) intensity at fixed latitude and latitude of a diffusivity maximum are two different things.

Decomposing the MMC transport term into dynamic and thermodynamic components, we find once again that it is dominated by the dynamic component of the change (cyan solid line, Figures 4c and 4d). Residual terms are often relatively small (black solid and dotted lines, Figures 4a–4d), as are those associated with stationary eddy MSE transport (blue line, Figures 4a and 4b) and nonlinearities in the H_{mmc} dynamic-thermodynamic decomposition (not shown). Overall, the difference between AQUA and AMIP in the diffusivity intensity response to SST change is quite striking.

As for the diffusivity shifts, the choice of a prescribed-SST or a slab ocean lower boundary condition for the atmosphere seems to have a larger effect on AQUA than on AMIP simulations. The AQUA-SO diffusivity intensification with warming is only about a third as large as in the corresponding AQUA experiment. The AQUA-SO total transport-related increase is 29% smaller, and the MSE gradient-related decrease is roughly 5 times larger, than their respective AQUA counterparts. The fact that the AMIP intensity response to SST change is relatively small in comparison to internal variability hides the fact that the AMIP-SO MMC-related intensification is 60% larger than in AMIP. However, the correlation of the AMIP and AMIP-SO values for the nine unique intensity change components shown in Figure 4 is 0.98—in contrast, it is 0.69 for AQUA and AQUA-SO.

Surface heat flux changes form a key component of the diffusivity increase across the full SST range (cyan dashed line, Figures 5a and 5b), although shortwave absorption becomes more important for AMIP experiments warmer than the control run (cyan solid line, Figures 5a and 5b). OLR changes (cyan dash-dot line, Figures 5a and 5b) oppose the diffusivity increase, qualitatively consistent with Planck feedback. The atmospheric energy storage and residual terms are small and have been combined (black dotted line, Figures 5a and 5b). It is possible to further subdivide the surface heat flux-related diffusivity changes—for AQUA latent energy fluxes (green solid line, Figures 5c and 5d) dominate at all SSTs. For AMIP, latent energy fluxes are generally the largest term in the global cooling response. Their global warming response is similar

MOORING AND SHAW 10 of 20

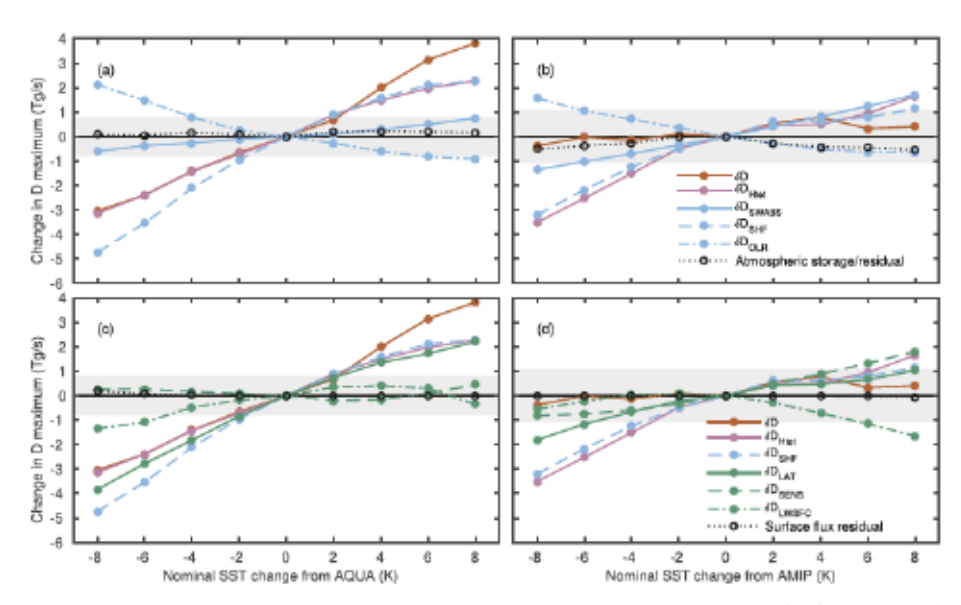


Figure 5. Roles of different MSE sources and sinks in diffusivity intensity change for AQUA (a, c) and AMIP (b, d) model configurations. The total transport-related change can be subdivided (a, b) into three components of energy input to the atmosphere and the sum of atmospheric energy storage and a residual. Red and magenta lines and gray shading are as in Figure 4. The surface heat flux-related change can be further subdivided (c, d) into latent heat, sensible heat, and surface longwave fluxes and another residual.

to the full surface heat flux-related diffusivity response, but this is due to strong compensation between sensible heat-related increases (green dashed line, Figures 5c and 5d) and surface longwave-related decreases (green dash-dot line, Figures 5c and 5d).

5. Implications of Diffusivity Change

In the previous section we established that the position and intensity of the midlatitude MSE diffusivity maximum varies with climate and investigated how these diffusivity changes are related to atmospheric thermodynamics and dynamics. We will now attempt to relate the diffusivity to two other midlatitude eddy activity metrics and quantify the impact of the diagnosed diffusivity changes on the climate of the EBM.

5.1. Links Between Diffusivity and Other Midlatitude Circulation Metrics

Ultimately, our aim is to connect diffusivity to other more traditional (or at least dynamics-oriented) metrics of storm track activity. As a first step in this direction, we examine the relationship between the maxima of diffusivity and EKE. Zonal-mean vertically integrated EKE was computed as a function of latitude following Shaw et al. (2018)—note that we are thus defining transient eddies using a high-pass filter with a 10-day cutoff (rather than by subtracting a monthly mean) for purposes of the EKE calculation. Identification of latitudes and intensities of maxima then proceeded as for diffusivity.

Clear and approximately linear relationships between the properties of the diffusivity and EKE maxima are found. The latitude of the zonal-mean EKE maximum is found to be well correlated with the diffusivity maximum (Figure 6a, r>0.94, p<0.0002 using a two-tailed t test) as are the diffusivity intensity and the magnitude of maximum zonal-mean EKE (Figure 6b, r>0.82, p<0.007 using a two-tailed t test). The strength of the dependence of the zonal-mean EKE maximum on the diffusivity maximum can differ substantially between AQUA and AMIP—for example, EKE increases nearly 5 times as much per unit of diffusivity increase for the latter than for the former. We also experimented with quantifying EKE using a zonal integral rather than a zonal mean—the two quantities are related by a factor of $2\pi a \cos \phi$. The most notable effect of this change on correlation values is reducing r for the AQUA EKE intensity from 0.94 to 0.81—for AQUA zonally integrated EKE is maximized in the +4 K experiment, rather than in the +8 K experiment as for zonal-mean EKE.

A disadvantage of the EKE diagnoses is the lack of a complete physical argument for the nature of the relationship between EKE and diffusivity. In contrast, Kushner and Held (1998) proposed that diffusivity (at least for lower tropospheric tracers) is proportional to the RMS eddy stream function in the same part

MOORING AND SHAW 11 of 20

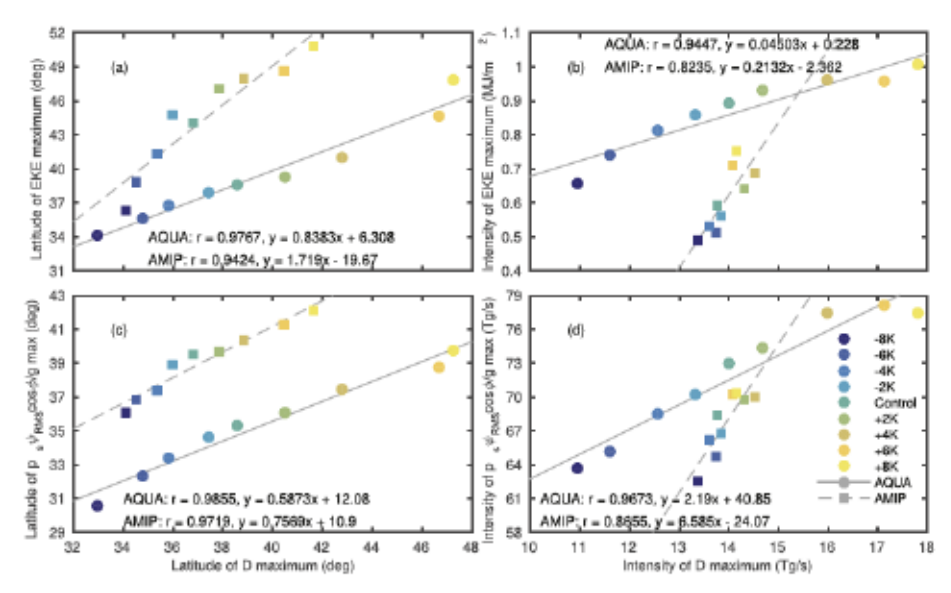


Figure 6. Relationships between the latitudes (a, c) and intensities (b, d) of maxima for diffusivity and other midlatitude eddy-related quantities. The diffusivity maxima are compared to those for zonal-mean eddy kinetic energy (a, b) and a rescaled form of the 925 hPa zonal-mean root-mean-square eddy stream function (c, d)—see main text for further details. Colored markers represent maxima diagnosed from individual AQUA and AMIP simulations, while lines are least squares fits. Equations for the least squares fit lines are given in each panel. The listed correlation values are associated with the raw diagnosed maxima, not the fits.

of the atmosphere, and supported this idea with an examination of the National Centers for Environmental Prediction/National Center for Atmospheric Research reanalysis data set. We thus also explore the relationship between our diagnostic diffusivity and the 925 hPa RMS eddy stream function, denoted ψ_{RMS} .

Inspired by Kushner and Held (1998), we postulate a scaling relationship

$$\left[\overline{m'\nu'}\right] \sim -\psi_{RMS}G$$
 (15)

where $\lceil \overline{m'v'} \rceil$ is the time mean zonal-mean transient eddy flux of MSE on the 925 hPa surface—m' and eddy meridional wind v' are defined as departures from time means as in Appendix A, although time and zonal means are now taken on pressure levels rather than model levels. We now more specifically define ψ_{RMS} as $\sqrt{|\psi'|^2}$. G is again the 925 hPa MSE gradient as defined in (2). Furthermore, we assume that

$$\frac{p_s}{g} \left[\overline{m'v'} \right] \sim \frac{H}{\cos \phi}$$
(16)

 p_s is the time mean zonal-mean surface pressure and thus the multiplication by p_s/g is a heuristic estimate of the vertically integrated eddy MSE transport. H is divided by $\cos \phi$ to transform it from a zonally integrated to a zonally averaged quantity and thus match $\left[\overline{m'v'}\right]$. By combining (15), (16), and the diffusivity definition (1), we get

$$D \sim \frac{p_s \psi_{RMS} \cos \phi}{g}$$
(17)

which suggests that D and ψ_{RMS} can be most readily compared if the latter is initially rescaled by a factor of $p_s \cos \phi/g$ —hereinafter we will generally refer to $p_s \psi_{RMS} \cos \phi/g$ as "rescaled ψ_{RMS} ".

As for EKE, the latitudes and intensities of the rescaled ψ_{RMS} maxima are approximately linearly related to the latitudes and intensities of the diffusivity maxima (Figures 6c and 6d). Note that the slopes of the least squares fit lines relating the latitudes of the D and rescaled ψ_{RMS} maxima deviate significantly from 1 (Figure 6c), which indicates that (17) cannot be made exact even within a single simulation. In other words, if there were some latitude-independent constant α by which D could be divided to yield $p_s\psi_{RMS}\cos\phi/g$ then the D and $p_s\psi_{RMS}\cos\phi/g$ maxima would be at exactly the same latitudes and the slope of the aforementioned

MOORING AND SHAW 12 of 20

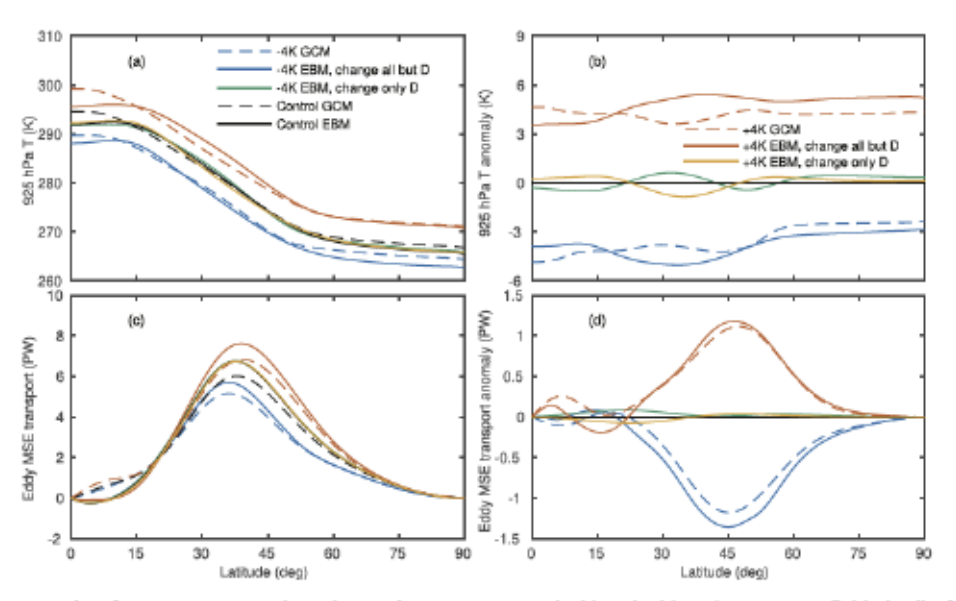


Figure 7. Results of attempts to reproduce the 925 hPa temperature (a, b) and eddy MSE transport fields (c, d) of three ECHAM6 AQUA simulations using an EBM with transient eddy MSE transport parameterized as diffusion. EBM outputs are shown with solid lines, while ECHAM6 output is shown with dashed lines. Both full fields (a, c) and anomalies relative to the control ECHAM6 and EBM simulations (b, d) are shown. See main text for further discussion, including a description of the two kinds of simulations performed with the EBM.

least squares fit line would be 1. It is not, and therefore no such α exists. However, D does at least provide order-of-magnitude accurate estimates of rescaled ψ_{RMS} for both AQUA and AMIP.

Overall, the EKE and rescaled ψ_{RMS} maxima vary with the diffusivity maxima in qualitatively quite similar ways. The previously mentioned greater sensivity of the EKE maximum intensity to diffusivity in AMIP than in AQUA carries over to rescaled ψ_{RMS} , albeit in a less extreme way. Furthermore, the latitudes of both the EKE and rescaled ψ_{RMS} maxima are more sensitive to variations in the latitude of the diffusivity maximum for AMIP than for AQUA.

5.2. Effects of Diffusivity Change on the Climate of an EBM

Finally, we investigate the effect of diffusivity change on the time mean atmospheric state and energy transports by using the EBM described in detail in section 2.2. First, we tune the EBM to achieve its best possible match to the ECHAM6 AQUA control simulation. Then we use the EBM to try to predict the ECHAM6 climate change responses to the nominal ± 4 K SST perturbations. We chose to analyze the ± 4 K AQUA simulations to maximize consistency with the Coupled Model Intercomparison Project phase 5 aqua4K experiments (e.g., Shaw & Voigt, 2016; Taylor et al., 2012). The EBM is able to skillfully reproduce the 925 hPa temperature and MSE transports of the AQUA control simulation (black lines, Figures 7a, 7c, 8a, and 8c). This is not surprising, because all relevant EBM input parameters were diagnosed from that same ECHAM6 simulation.

For each EBM version (D or D_{tot}) we attempted to use two different types of EBM experiment to reproduce each perturbed ECHAM6 simulation. The first type ("change all but D/D_{tot} ") has all input parameters except the diffusivity taken from the associated ± 4 K ECHAM6 simulation. For this type of EBM simulation, the diffusivity field is taken from the ECHAM6 control run. The second type of EBM experiment ("change only D/D_{tot} ") takes the diffusivity from the associated ± 4 K ECHAM6 simulation and all other inputs from the control ECHAM6 simulation.

The "change all but D/D_{tot} " experiments do a reasonable job reproducing the ± 4 K ECHAM6 simulations (blue and red lines, Figures 7a, 7c, 8a, and 8c)—thus the diffusivity changes are apparently not of great importance for the SST perturbation response, although the MSE transports in the EBM tend to be biased high in midlatitudes. In stark contrast, the output of the "change only D/D_{tot} " EBM experiments is only minimally different from that of the EBM experiments aimed at reproducing the ECHAM6 control run (green and gold lines, Figures 7a, 7c, 8a, and 8c). In other words, diffusivity changes alone do not do much to manifest the SST perturbation-related changes seen in 925 hPa temperature and MSE transport. To make

MOORING AND SHAW 13 of 20

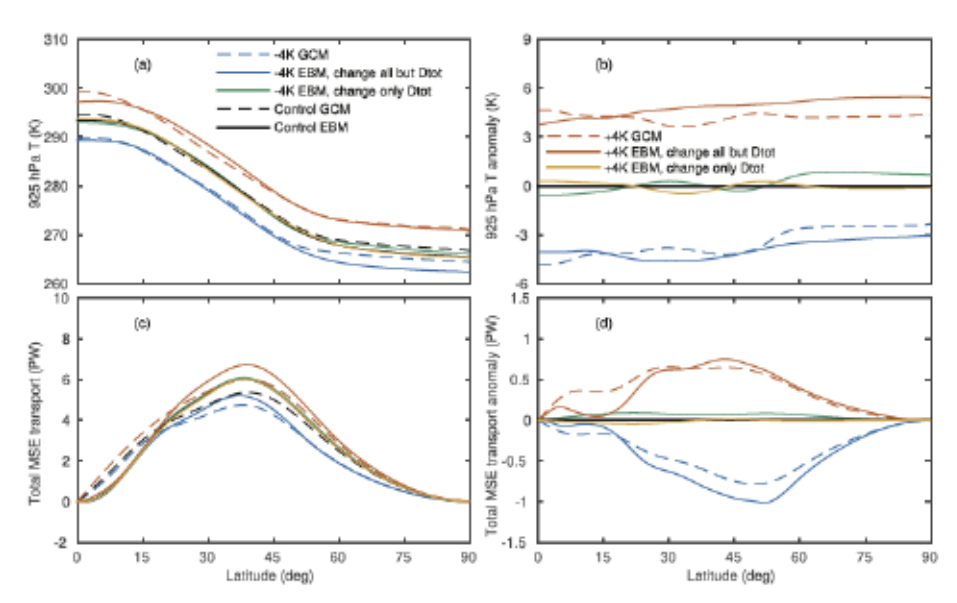


Figure 8. Similar to Figure 7 but using an EBM with the total MSE transport parameterized as diffusion. The plotted MSE transports (c) and transport anomalies (d) are thus totals over all circulation components, instead of just the transient eddy component as in Figure 7.

the changes or lack thereof easier to see and to minimize the effect of EBM biases, we also present the results in anomaly form (Figures 7b, 7d, 8b, and 8d). Cooling in the -4 K experiments is seen to be smallest in the polar regions—this is likely associated with the minimum in allowed SST mentioned in section 3.

In sum, the EBM experiments experiments suggest that diffusivity changes are of little significance for producing the time mean temperature and MSE transport responses to SST change. However, an important caveat must be attached to this result: while the EBM takes most components of the net MSE generation rate as specified inputs, MSE generation rates in ECHAM6 are determined internally by more fundamental inputs such as SSTs and the composition of the atmosphere. Thus, our EBM analysis cannot exclude the possibility that the atmospheric circulation changes embodied in the diffusivity also act to modulate MSE generation rates—in other words, there could be feedbacks between diffusivity and MSE generation not representable in this EBM.

6. Discussion and Conclusion

To explore the extent to which the midlatitude atmospheric circulation response to climate change can be understood in terms of the energy budget (Barpanda & Shaw, 2017; Shaw et al., 2018) and thermodynamically predictable changes in the mean state (Shaw & Voigt, 2016), we have defined a new diagnostic diffusivity framework. The diffusivity is computed as the negative of the ratio of the meridional transport of MSE by transient eddies to the time mean zonal-mean 925 hPa meridional gradient of MSE. Both quantities are taken from the output of general circulation model simulations. By manipulating the equations that define the diffusivity, we can decompose its response to climate change into components associated with various aspects of the atmospheric thermodynamic state and time mean flow.

Each component of the decomposition can be identified as thermodynamic or dynamic in nature, where thermodynamic (dynamic) components can (cannot) be computed without explicit reference to changes in the wind and surface pressure fields. Thermodynamic components of diffusivity change thus include those associated with changes in total MSE transport, 925 hPa MSE gradient, and the time mean zonal-mean MSE field advected by the mean meridional circulation (MMC). Dynamic components include those related to changes in the MMC's flow field (winds and surface pressures) and in stationary eddies. Our diffusivity diagnostic extends the work of Barpanda and Shaw (2017) and Shaw et al. (2018): By adding MSE gradient information, we more clearly separate circulation changes from changes in the mean thermodynamic state—these two categories of changes are mixed together in their work.

We use the new diffusivity framework to interpret prescribed-SST aquaplanet and AMIP experiments performed with the ECHAM6 AGCM. There is typically a midlatitude diffusivity maximum, which shifts

MOORING AND SHAW 14 of 20

poleward with increasing SST. This finding is consistent with published results on the storm track response to global warming in coupled climate models (e.g., Chang et al., 2012; Shaw et al., 2016; Yin, 2005) and with diffusivity shifts in additional slab ocean simulations we performed.

In agreement with the results of Shaw and Voigt (2016), changes in time mean zonal-mean MSE gradient in response to global warming promote the poleward diffusivity shift. We find this component of the shift to be primarily due to strengthening of the latent energy gradient. The diagnosed shift for the AMIP +4 K experiment is larger than that reported by Barpanda and Shaw (2017) because their result neglects the MSE gradient contribution. This revised result illustrates the value of accounting for gradient-related diffusivity shifts.

We evaluated whether the MSE gradient-related diffusivity shifts could be explained in terms of Clausius-Clapeyron changes in specific humidity. An assumption that relative humidity remains fixed at climatological values yields reasonable predictions of such shifts. However global-mean temperature change does not control these shifts, instead changes in temperature gradient are important. There is a clear feedback between the circulation and atmospheric meridional temperature gradient even in prescribed-SST experiments as pointed out by Shaw and Voigt (2016) for aquaplanet simulations—we have generalized their result by showing that it also applies to AMIP simulations.

Changes in MSE transport by the MMC, primarily associated with changes in the Ferrel cell, also constitute an important component of the total diffusivity shift. The Ferrel cell-related diffusivity shift implies a link between the momentum budget and our MSE budget-based diffusivity since the Coriolis torque on the upper branch of the Ferrel cell is balanced by transient eddy momentum flux convergence (Schneider, 2006). Unfortunately, this reduces the utility of the diffusivity framework because changes in eddy momentum fluxes cannot be predicted in any obvious way from thermodynamic or radiative arguments—thus better understanding of the Ferrel cell component requires a connection between the MSE and momentum budgets. A recent study by Lachmy and Shaw (2018) made progress in this direction but more work is needed. Alternatively, one could transform to isentropic coordinates to remove the Ferrel circulation but this complicates the surface boundary condition (Held & Schneider, 1999; Pauluis et al., 2008).

Diffusivity intensity increases much more overall for AQUA than for AMIP in response to increasing SST, despite several qualitative similarities between the model configurations in the individual components of diffusivity change. Thermodynamic processes are important—increases in total MSE transport with SST are associated with diffusivity increases, while MSE gradient changes are associated with diffusivity reductions. Changes in surface heat fluxes (particularly latent heat flux) are a major positive component of the diffusivity increase for both the AQUA and AMIP simulations, while outgoing longwave radiation changes oppose it. These results on the contributions of specific MSE sources and sinks agree with those of Shaw et al. (2018) for the AMIP +4 K experiment—however in contrast to Shaw et al. (2018) we find a relatively small total increase because we also account for the diffusivity reduction associated with MSE gradient change. The stronger response in AQUA than in AMIP is primarily linked to opposite signs of the MMC-related response to cooling and differences in total transport- and gradient-related responses to warming.

To relate our diagnostic diffusivity to more traditional storm track metrics, we compared the diffusivity maxima to maxima of vertically integrated EKE and a form of the 925 hPa RMS eddy stream function that has been rescaled to be more diffusivity-like. Strongly positive correlations between the properties of the maxima of diffusivity and these other dynamical quantities were found. However, the sensitivity of the EKE or rescaled RMS eddy stream function maximum properties to changes in the diffusivity maximum depends on the model configuration—they are more sensitive to diffusivity change in AMIP than in AQUA, for reasons unknown.

Finally, we investigated the implications of diffusivity variations for large-scale climate change using a modified version of the Hwang and Frierson (2010) EBM. We found them to have little impact on the EBM's solutions—this result highlights the important disconnect between the zonally symmetric thermodynamic and dynamic responses to climate change, which has been noted previously (Shepherd, 2014).

Several more advancements would need to be made to enable use of our diffusivity framework as a closed theory of zonally symmetric storm track responses to climate change. To predict the diffusivity shifts, some external theory for the changes in the Ferrel cell flow would be particularly helpful. Further understanding

MOORING AND SHAW 15 of 20

is needed of why low-level temperature gradients change with SST, even when the meridional gradient of SST is held fixed—however, fixed relative humidity appears to be a fairly accurate theory of specific humidity change. To predict changes in diffusivity intensity it might be useful to compute changes in the net energy input to the atmosphere via radiative or thermodynamic arguments. Additional work is also needed to understand why the linear relationships between the maxima of diffusivity and other eddy dynamical quantities are as they are. While there is still much to be done, the MSE diffusivity is clearly a useful concept that helps to link the climate change response of the midlatitude circulation to the atmospheric energy budget and mean thermodynamic state.

Appendix A: Energy Transport Calculation on Model Levels

We experimented with calculating MSE transports on both pressure and model levels for the AQUA control and +4 K simulations, and opted to use transports on model levels in all of our analyses because of problems in accurately computing the MSE transports on pressure levels at low latitudes. The problems appear to arise because the total MSE transport involves sums of pairs of large terms of opposite sign (dry static and latent energy, sensible and geopotential components of dry static energy). However, decomposition of the flow into a mean meridional circulation, stationary eddies, and transient eddies is harder in ECHAM6's native vertical coordinate because it transitions from sigma near the surface to pressure at higher altitudes.

Extending the notation of the main paper, we denote the pressure thickness of a single model layer by Δp . Δp (as well as m and meridional wind v, of course) can vary in space and time. For some quantity x, the unweighted time mean at fixed horizontal position in a given model layer is then \overline{x} and the mass-weighted time mean is

$$\tilde{x} = \frac{\overline{x\Delta p}}{\overline{\Delta p}} \tag{A1}$$

Transient eddies are $x' = x - \tilde{x}$, and stationary waves are

$$x^{\dagger} = \tilde{x} - \frac{\left[\overline{x\Delta p}\right]}{\left[\overline{\Delta p}\right]}$$
 (A2)

where [x] is the zonal mean of x. For clarity, $[x] = \frac{1}{2x} \int_0^{2x} x d\lambda$, where λ is the longitude.

By these definitions, the time mean zonally integrated meridional transport of MSE within a single model layer is $(2\pi a \cos \phi/g) \left[\overline{mv\Delta p} \right]$, where a, ϕ and g are as defined in the main paper. It can be shown that

$$\left[\overline{mv\Delta p}\right] = \frac{\left[\overline{m\Delta p}\right]\left[\overline{v\Delta p}\right]}{\left[\overline{\Delta p}\right]} + \left[m^{\dagger}v^{\dagger}\overline{\Delta p}\right] + \left[\overline{m'v'\Delta p}\right]$$
(A3)

The three terms on the right hand side of the equation can clearly be identified with the mean meridional circulation and the stationary and transient eddies, respectively, similar to (4). Thus, for example,

$$H = \frac{\cos \phi}{g} \sum_{i=1}^{47} \left[\overline{m'v'\Delta p} \right]_i \tag{A4}$$

where the sum is over all 47 levels of the model and H is normalized as described in section 2.1.

It is also worth explicitly clarifying the definition of the time mean. For the analyses presented in this paper, time means were computed over individual months (e.g., yielding 120 total monthly means for each AQUA simulation). This choice is appropriate because the most obvious alternative, taking time means over the entire length of each AQUA simulation or all 30 years of a given month in an AMIP simulation, would result in extremely low-frequency variability becoming included in the definition of transient eddies. When needed, seasonal-mean transports were then computed as means of monthly transports.

MOORING AND SHAW 16 of 20

Appendix B: Dynamic and thermodynamic components of MMC MSE transport changes

Separation of changes in H_{mmc} into components associated with changes in dynamics (meridional wind and surface pressure) and thermodynamics (time mean zonal-mean MSE) is performed as follows: Using the notation described in the previous appendix, we define the time mean zonal-mean MSE transport (up to a factor of g) associated with the mean meridional circulation for a single model layer as

$$\hat{H}_{mmc} = \frac{\left[\overline{m\Delta p}\right]\left[\overline{\nu\Delta p}\right]}{\left[\overline{\Delta p}\right]} \tag{B1}$$

Using subscripts p and c to denote quantities evaluated from the output of perturbation and control simulations, respectively, it is readily seen that

$$\hat{H}_{mmc,p} - \hat{H}_{mmc,c} = \frac{\left[\overline{m_p \Delta p_p}\right] \left[\overline{v_p \Delta p_p}\right]}{\left[\overline{\Delta p_p}\right]} - \frac{\left[\overline{m_c \Delta p_c}\right] \left[\overline{v_c \Delta p_c}\right]}{\left[\overline{\Delta p_c}\right]}$$
(B2)

We can also write

$$\hat{H}_{mmc,p} - \hat{H}_{mmc,c} = \Delta \hat{H}_{mmc,dyn} + \Delta \hat{H}_{mmc,thr} + \Delta \hat{H}_{mmc,nln}$$
 (B3)

where

$$\Delta \hat{H}_{mmc,dyn} = \frac{\left[\overline{m_c \Delta p_p}\right] \left[\overline{v_p \Delta p_p}\right]}{\left[\overline{\Delta p_p}\right]} - \hat{H}_{mmc,c} \tag{B4}$$

$$\Delta \hat{H}_{mmc,thr} = \frac{\left[\overline{m_p \Delta p_c}\right] \left[\overline{v_c \Delta p_c}\right]}{\left[\overline{\Delta p_c}\right]} - \hat{H}_{mmc,c} \tag{B5}$$

and (B3) defines $\Delta \hat{H}_{mmc,nln}$ as a nonlinear term. Physically, it is clear that $\Delta \hat{H}_{mmc,dyn}$ is associated with changes in dynamics at fixed time mean zonal-mean MSE and $\Delta \hat{H}_{mmc,thr}$ is associated with changes in the thermodynamic state at fixed flow. These terms underlie the $\delta D_{Hmmc,dyn}$ and $\delta D_{Hmmc,thr}$ lines of Figures 2 and 4. We do not show a $\delta D_{Hmmc,nln}$ line in either figure because this term is small in both cases.

Appendix C: Diagnosing sources of change in midlatitude diffusivity maxima

Here we more formally present the method for associating changes in the position or intensity of a midlatitude diffusivity maximum with changes in the various MSE transport and gradient components. Barpanda and Shaw (2017) and Shaw et al. (2018) employ it to analyze changes in the position and intensity of a storm track defined using eddy MSE transport, however the method is applicable without change to analyses of diffusivity.

Our initial exposition of how changes in H and G yield changes in D was done in the limit of infinitesimal changes. Now let us more rigorously define finite-amplitude diffusivity changes: denoting climatological quantities with $\{\cdot\}$ and perturbed quantities with $\langle\cdot\rangle$, we can write

$$\Delta D = \Delta D_{tt} + \Delta D_{C}$$
 (C1)

where

$$\Delta D_H = -\frac{(\langle H \rangle - \{H\})}{\{G\}}$$
 (C2)

$$\Delta D_G = \frac{\{H\} \left(\langle G \rangle - \{G\} \right)}{\{G\}^2} \tag{C3}$$

MOORING AND SHAW 17 of 20

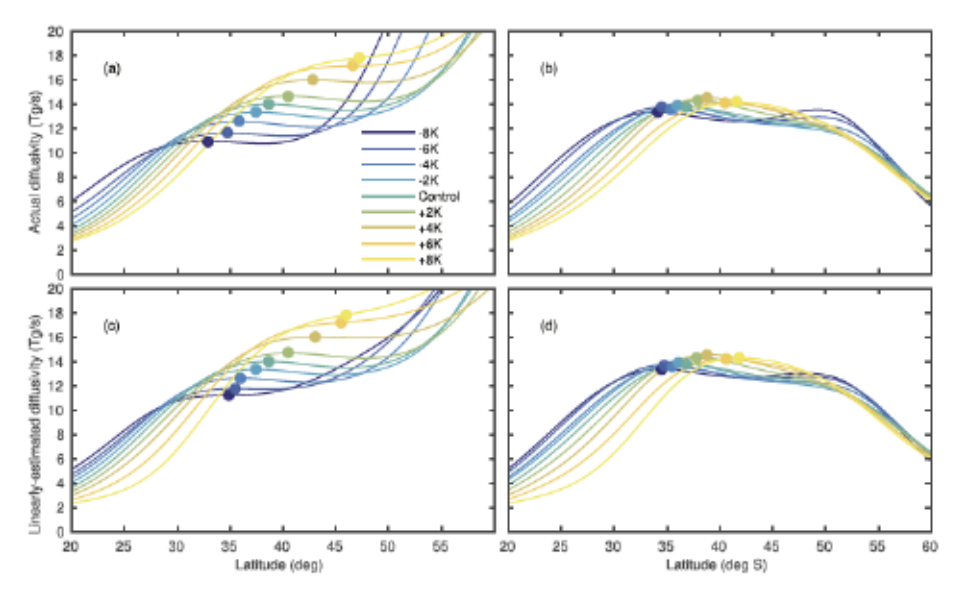


Figure C1. Diagram of the diffusivity maximum shift and intensity change analysis process for the AQUA (a, c) and AMIP (b, d) model configurations. The top row shows actual diffusivity profiles $\langle D \rangle$, while the bottom row shows the linearly estimated perturbed diffusivity profiles $\{D\} + \Delta D$. By definition, the control run diffusivity profiles are exactly the same in both rows. The circles mark the identified midlatitude local maxima, or latitudes at which the magnitude of the meridional slope of the diffusivity is minimized if no maximum exists in the latitude range of interest. Note the slight variations in marker positions between the top and bottom rows of this figure—this is associated with $\Delta \mathcal{M}_{RLA}$ as defined in (C8).

and ΔD_H and ΔD_G can be further subdivided as outlined in section 2.1. Note that under these definitions ΔD is only approximately the difference between $\langle D \rangle$ and $\{D\}$: by combining (1) and (C1-C3) we can show that in fact

$$\langle D \rangle = \{D\} + \frac{\{G\}}{\langle G \rangle} \Delta D$$
 (C4)

We further denote the latitude or intensity of the midlatitude diffusivity maximum from some diffusivity profile D_j as $\mathcal{M}\left(D_j\right)$. The $\mathcal{M}\left(\cdot\right)$ maximum search operation is implemented numerically as a calculation of the latitude at which $\partial D_j/\partial \phi=0$, with $\partial D_j/\partial \phi$ estimated using finite differences from data on a 0.1° grid. We restrict the latitude range of the maximum search and deal with the possibility that there is no maximum as described in section 2.1. For a diffusivity perturbation ΔD_m (i.e., ΔD or a subdivision thereof) relative to a climatological state, we define the shift of the latitude of the maximum or the change of its magnitude as

$$\Delta \mathcal{M} (\Delta D_m) = \mathcal{M} (\{D\} + \Delta D_m) - \mathcal{M} (\{D\})$$
 (C5)

where $\{D\}$ is in this context the actual diffusivity in the relevant control simulation. This definition is illustrated in Figure C1.

Because the maximum search operation is intrinsically nonlinear, the shifts or maximum magnitude changes associated with two different diffusivity perturbations ΔD_m and ΔD_n will not necessarily sum up to the response to both perturbations applied simultaneously—at best we will have $\Delta \mathcal{M} \left(\Delta D_m + \Delta D_n \right) \approx \Delta \mathcal{M} \left(\Delta D_m \right) + \Delta \mathcal{M} \left(\Delta D_n \right)$. We can thus define a "nonlinearity residual" as

$$\Delta M_{RNL} (\Delta D_m, \Delta D_n) = \Delta M (\Delta D_m + \Delta D_n) - \Delta M (\Delta D_m) - \Delta M (\Delta D_n)$$
 (C6)

Note also that for analyses of this nature to be meaningful we need

$$\mathcal{M}(\langle D \rangle) - \mathcal{M}(\{D\}) \approx \Delta \mathcal{M}(\Delta D)$$
 (C7)

where $\langle D \rangle$ is the actual diffusivity in the perturbed simulation. We cannot assume that (C7) will be exactly satisfied, because the assumption made in (C5) that $\{G\}/\langle G \rangle = 1$ is only approximately correct. We therefore define a "linear/actual residual" as

$$\Delta M_{RIA} = M(\langle D \rangle) - M(\{D\}) - \Delta M(\Delta D)$$
 (C8)

MOORING AND SHAW 18 of 20



The residuals plotted in Figures 2a, 2b, 4a, and 4b are $\Delta \mathcal{M}_{RNL} + \Delta \mathcal{M}_{RLA}$, while those plotted in Figures 2c, 2d, 3a, 3b, 4c, 4d, 5c, and 5d are just $\Delta \mathcal{M}_{RNL}$. The residual component of the atmospheric storage/residual term in Figures 5a and 5b is also $\Delta \mathcal{M}_{RNL}$.

Acknowledgments

T. A. M. and T. A. S. are supported by the David and Lucile Packard Foundation. The ECHAM6 simulations in this paper were completed with resources provided by the University of Chicago Research Computing Center. Data and code necessary to reproduce the figures in this paper are available via the University of Chicago's institutional repository Knowledge@Uchicago (at https://doi.org/10.6082/uchicago.2055). Comments from Rodrigo Caballero and several anonymous reviewers substantially improved the paper.

References

- Barpanda, P., & Shaw, T. (2017). Using the moist static energy budget to understand storm-track shifts across a range of time scales. Journal of the Atmospheric Sciences, 74(8), 2427–2446. https://doi.org/10.1175/JAS-D-17-0022.1
- Barry, L., Craig, G. C., & Thuburn, J. (2002). Poleward heat transport by the atmospheric heat engine. Nature, 415(6873), 774–777. https://doi.org/10.1038/415774a
- Chang, E. K. M., Guo, Y., & Xia, X. (2012). CMIP5 multimodel ensemble projection of storm track change under global warming. *Journal of Geophysical Research*, 117, D23118. https://doi.org/10.1029/2012JD018578
- Donohoe, A., & Battisti, D. S. (2013). The seasonal cycle of atmospheric heating and temperature. *Journal of Climate*, 26(14), 4962–4980. https://doi.org/10.1175/JCLI-D-12-00713.1
- Flannery, B. P. (1984). Energy balance models incorporating transport of thermal and latent energy. Journal of the Atmospheric Sciences, 41(3), 414–421. https://doi.org/10.1175/1520-0469(1984)041<0414:EBMITO>2.0.CO;2
- Frierson, D. M. W., Held, I. M., & Zurita-Gotor, P. (2007). A gray-radiation aquaplanet moist GCM Part II: Energy transports in altered climates. Journal of the Atmospheric Sciences, 64(5), 1680–1693. https://doi.org/10.1175/JAS3913.1
- Gates, W. L. (1992). AMIP: The atmospheric model intercomparison project. Bulletin of the American Meteorological Society, 73(12), 1962–1970. https://doi.org/10.1175/1520-0477(1992)073<1962:ATAMIP>2.0.CO;2
- Grise, K. M., & Polvani, L. M. (2014). The response of midlatitude jets to increased CO₂: Distinguishing the roles of sea surface temperature and direct radiative forcing. Geophysical Research Letters, 41, 6863–6871. https://doi.org/10.1002/2014GL061638
- He, J., Soden, B. J., & Kirtman, B. (2014). The robustness of the atmospheric circulation and precipitation response to future anthropogenic surface warming. Geophysical Research Letters. 41, 2614–2622. https://doi.org/10.1002/2014GL059435
- Held, I. M. (2005). The gap between simulation and understanding in climate modeling. Bulletin of the American Meteorological Society, 86(11), 1609–1614. https://doi.org/10.1175/BAMS-86-11-1609
- Held, I. M., & Larichev, V. D. (1996). A scaling theory for horizontally homogeneous, baroclinically unstable flow on a beta plane. Journal of the Atmospheric Sciences, 53(7), 946–952. https://doi.org/10.1175/1520-0469(1996)053<0946:ASTFHH> 2.0.CO;2
- Held, I. M., & Schneider, T. (1999). The surface branch of the zonally averaged mass transport circulation in the troposphere. Journal of the Atmospheric Sciences, 56(11), 1688–1697. https://doi.org/10.1175/1520-0469(1999)056<1688:TSBOTZ>2.0.CO;2
- Held, I. M., & Soden, B. J. (2006). Robust responses of the hydrological cycle to global warming. *Journal of Climate*, 19(21), 5686–5699. https://doi.org/10.1175/JCLI3990.1
- Hwang, Y., & Frierson, D. M. W. (2010). Increasing atmospheric poleward energy transport with global warming. Geophysical Research Letters, 37, L24807. https://doi.org/10.1029/2010GL045440
- Kushner, P. J., & Held, I. M. (1998). A test, using atmospheric data, of a method for estimating oceanic eddy diffusivity. Geophysical Research Letters, 25(22), 4213–4216. https://doi.org/10.1029/1998GL900142
- Lachmy, O., & Shaw, T. (2018). Connecting the energy and momentum flux response to climate change using the Eliassen-Palm relation. Journal of Climate, 31(18), 7401–7416. https://doi.org/10.1175/JCLI-D-17-0792.1
- Neale, R. B., & Hoskins, B. J. (2000). A standard test for AGCMs including their physical parametrizations: I: The proposal. Atmospheric Science Letters, I(2), 101–107. https://doi.org/10.1006/aslc.2000.0022
- Neelin, J. D., & Held, I. M. (1987). Modeling tropical convergence based on the moist static energy budget. Monthly Weather Review, 115(1), 3–12. https://doi.org/10.1175/1520-0493(1987)115<0003:MTCBOT>2.0.CO;2
- O'Gorman, P. A. (2010). Understanding the varied response of the extratropical storm tracks to climate change. Proceedings of the National Academy of Sciences, 107(45), 19,176–19,180. https://doi.org/10.1073/pnas.1011547107
- Pauluis, O., Czaja, A., & Korty, R. (2008). The global atmospheric circulation on moist isentropes. Science, 321(5892), 1075–1078. https://doi.org/10.1126/science.1159649
- Pierrehumbert, R. T. (2005). Climate dynamics of a hard snowball Earth. Journal of Geophysical Research, 110, D01111. https://doi.org/10.1029/2004JD005162
- Sardeshmukh, P. D., & Hoskins, B. I. (1984). Spatial smoothing on the sphere. Monthly Weather Review, 112(12), 2524–2529. https://doi.org/10.1175/1520-0493(1984)112<2524:SSOTS>2.0.CO;2
- Schneider, T. (2006). The general circulation of the atmosphere. Annual Review of Earth and Planetary Sciences, 34(1), 655–688. https://doi.org/10.1146/annurev.earth.34.031405.125144
- Seager, R., Naik, N., & Vecchi, G. A. (2010). Thermodynamic and dynamic mechanisms for large-scale changes in the hydrological cycle in response to global warming. *Journal of Climate*, 23(17), 4651–4668. https://doi.org/10.1175/2010JCLJ3655.1
- Sellers, W. D. (1969). A global climatic model based on the energy balance of the Earth-atmosphere system. Journal of Applied Meteorology, 8(3), 392–400. https://doi.org/10.1175/1520-0450(1969)008<0392:AGCMBO>2.0.CO;2
- Shaw, T. A. (2019). Mechanisms of future predicted changes in the zonal mean mid-latitude circulation. Current Climate Change Reports, 5(4), 345–357. https://doi.org/10.1007/s40641-019-00145-8
- Shaw, T. A., Baldwin, M., Barnes, E. A., Caballero, R., Garfinkel, C. I., Hwang, Y.-T., et al. (2016). Storm track processes and the opposing influences of climate change. Nature Geoscience, 9, 656–664. https://doi.org/10.1038/ngeo2783
- Shaw, T. A., Barpanda, P., & Donohoe, A. (2018). A moist static energy framework for zonal-mean storm-track intensity. Journal of the Atmospheric Sciences, 75(6), 1979–1994. https://doi.org/10.1175/JAS-D-17-0183.1
- Shaw, T. A., & Voigt, A. (2016). What can moist thermodynamics tell us about circulation shifts in response to uniform warming? Geophysical Research Letters, 43, 4566–4575. https://doi.org/10.1002/2016GL068712
- Shepherd, T. G. (2014). Atmospheric circulation as a source of uncertainty in climate change projections. Nature Geoscience, 7, 703–708. https://doi.org/10.1038/ngeo2253
- Simpson, I. R., Shaw, T. A., & Seager, R. (2014). A diagnosis of the seasonally and longitudinally varying midlatitude circulation response to global warming. Journal of the Atmospheric Sciences, 71(7), 2489–2515. https://doi.org/10.1175/JAS-D-13-0325.1
- Stevens, B., Giorgetta, M., Esch, M., Mauritsen, T., Crueger, T., Rast, S., et al. (2013). Atmospheric component of the MPI-M Earth System Model: ECHAM6. Journal of Advances in Modeling Earth Systems, 5, 146–172. https://doi.org/10.1002/jame.20015

MOORING AND SHAW 19 of 20





- Stone, P. H. (1973). The effect of large-scale eddies on climatic change. Journal of the Atmospheric Sciences, 30(4), 521–529. https://doi.org/10.1175/1520-0469(1973)030<0521:TEOLSE>2.0.CO;2
- Taylor, K. E., Stouffer, R. J., & Mechl, G. A. (2012). An overview of CMIP5 and the experiment design. Bulletin of the American Meteorological Society, 93(4), 485–498. https://doi.org/10.1175/BAMS-D-11-00094.1
- Vallis, G. K., Zurita-Gotor, P., Cairns, C., & Kidston, J. (2015). Response of the large-scale structure of the atmosphere to global warming. Quarterly Journal of the Royal Meteorological Society, 141(690), 1479–1501. https://doi.org/10.1002/qj.2456
- Yin, J. H. (2005). A consistent poleward shift of the storm tracks in simulations of 21st century climate. Geophysical Research Letters, 32, L18701. https://doi.org/10.1029/2005GL023684

MOORING AND SHAW 20 of 20